Cite this: DOI: 00.0000/xxxxxxxxxx

Pressure-controlled formation of discontinuous clogs in tapered microchannels †

Olukayode T. Majekodunmi [a] and Sara M. Hashmi *[abc]

Received Date
Accepted Date

DOI: 00.0000/xxxxxxxxxx

In suspension flows through microchannels with parallel walls, rigid particles form clogs that grow continuously in the upstream direction. However, introducing a slight taper to channel walls leads to a qualitatively different clogging mechanism. Clogs of rigid particles do not grow continuously in these tapered pores. Instead, new clogs form upstream of pre-existing clogs, truncating their growth, and thereby creating multiple distinct clogs within a channel. We refer to this novel phenomenon as discontinuous clogging. Here, we investigate its features by analyzing the dimensions and locations of discontinuous clogs in parallel tapered pores. Measurements reveal the discontinuity of clog growth depends strongly on flow driving pressure and particle volume fraction. Increasing volume fraction increases clogging frequency and positions the clogs upstream, in wider regions of the channels. Two regimes of driving pressure appear to exist as the discontinuous clogs are observed to become dramatically longer above a critical pressure. Interestingly, these long clogs are located downstream, towards the channel outlet, at the lowest volume fraction. However, they are increasingly located upstream as volume fraction increases. The dependence of clog location on pressure and volume fraction lends insight into bridging mechanism. Particles arriving simultaneously to a given location can span the channel width to form a bridge, which happens easily at higher volume fractions. Permanent clogs form when driving pressure is lower than the force the bridges can sustain. As driving pressure increases, however, it can overcome the force chains, preventing formation of new permanent clogs, and pushing particles further downstream.

1 Introduction

Clogging is frequently encountered in industrial processes, subsurface systems, and water treatment facilities [1,2]. The presence of suspended particles in these confined flow systems often results in the formation of clogs, which grow as more suspension flows through the channel [3]. Clog formation causes a decrease in suspension flowrate at constant driving pressures [4–7]. It can also increase the driving pressure required to maintain a constant flowrate [8]. Particulate or colloidal clogging in flow systems can result in catastrophic failure. In severe cases, it can cause complete flow stoppage and plant shutdown. It is a major driver for cost and energy use in many process industries.

Although clogging is an undesirable random event in many applications, it is the working principle of filtration systems [9,10]. It is also the reason for their eventual failure. Filters contain a network of pores and channels designed to remove suspended particles while the filtrate flows through [11]. As such, the rate of clogging determines the lifetime of a filter. Clogging has also been employed in disease diagnostics and cell sorting based on the size, shape and deformability of cells in narrow confinements [12]. These applications are made possible by advancements in microfluidic technologies.

Clogging occurs in confined flows through three main mechanisms: sieving, bridging and adhesion. Microfluidic platforms facilitate isolating and investigating these mechanisms. The simplest involves single particles sieving into constrictions of approximately the same size as the flowing particles [13]. Clogs can also form by bridging in larger constrictions [14,15]. Here, arches of two or more particles form across the width of the constriction, stabilized by force chains [16,17]. Bridges are formed when multiple particles attempt to navigate a constriction simultaneously. Flow stoppage due to bridging occurs in both dense and dilute suspensions. Both particle volume fraction and constriction width determine the probability of bridge formation. For particle volume fractions near the jamming fraction of ∼60% and as low as 0.5% [15,18], steric effects are sufficient to cause both sieving and bridging. Up to five particles participate in a bridge, in both constricted granular and suspension flows [19–21]. Clogging can also be induced by attractive interactions between the particles and the pore walls [22,23]. Clogging by deposition can be induced or prevented by surface treatments of the channels walls. Increasing the ionic strength of the suspension, for instance particle dispersion in NaCl solution, can induce inter-particle aggregation and wall deposition [18].

Colloidal interactions, hydrodynamic and contact forces play competitive roles in the formation, stability and growth of clogs [24–27]. This competition leads to critical phenomena in clogging processes. In a cross-flow setup, adjusting viscosity and flowrate can prevent clogging by deposition at the intersection [25]. Below a critical value of the hydrodynamic stress, particles de-

---

[a] *Department of Chemical Engineering, Northeastern University, Boston, MA 02115.*

[b] *Department of Mechanical & Industrial Engineering, Northeastern University, Boston, MA 02115.*

[c] *Department of Chemistry & Chemical Biology, Northeastern University, Boston, MA 02115; E-mail: s.hashmi@northeastern.edu*

† Electronic Supplementary Information (ESI) available.

https://doi.org/10.26434/chemrxiv-2023-nfmkc-v2 **ORCID:** https://orcid.org/0000-0002-9773-6748 Content not peer-reviewed by ChemRxiv. **License:** CC BY 4.0

posit on the channel walls, eventually forming a permanent clog. In a system of parallel microchannels with driving pressures ≤ 20 mbar, flow is too low to overcome attractive colloidal forces that induce clogging by adhesion[26]. Above 20 mbar, high driving pressure delays clogging. The number of particles escaping the channels before clogging increases with increasing pressure. In addition, Lattice Boltzmann simulations of suspension flow through pores show that clogs formed by adhesion can be removed using driving pressures higher than a critical value[28]. This critical behavior can also manifest as a function of flux density[29], number of injected pore volumes[23], and coulombic repulsion[30].

Besides steric effects and surface interactions, channel geometry also significantly impacts the rate and pattern of clogging by suspended particles[31–35]. In pores with parallel walls, clogs grow continuously from their points of inception, leading to a linear decay of flowrate with time[4]. Although increasing the entrance angle of approach to a pore can decrease clogging rates, it does not alter the continuous nature of clog growth[32]. However, in pores that gently taper over multiple length scales in the flow direction, flowrate decays much more gradually with time[4]. This results from the discontinuous growth of clogs: the growth of a downstream clog ends when a new clog is initiated immediately upstream. It shows the nature of clog formation and growth determines the details of subsequent decays in flowrate.

Tapered geometries are typically found in nozzles – for example, in 3D printers, injectors and extruders[36]. It could summarize flow dynamics in systems where the cross-sectional area decreases along the flow path such as in multi-stage filtration systems and blood circulation. Also, investigating clogging in gently tapered channels facilitates measurements of clog formation over a range of particle size to pore width ratios. This work describes such in a system of 165 parallel tapered channels. The channels are all connected to one inlet reservoir, and each tapers gently from inlet to outlet at a constant angle. The channel inlets are 10 particle diameters wide while the outlets are the same size as the particles. Thus, the particles do not escape the channels.

Suspension flow is driven through the parallel tapered channels at constant pressures, over a range of particle volume fractions and driving pressures. It is worth noting that the range of ΔP explored in this study spans, approximately, an order of magnitude greater than common values in related, pressure-driven studies[13,32]. The number, dimensions, and position of clogs in the channels are controlled by both driving pressure and particle volume fraction.

This tapered geometry allows the simultaneous investigation of clogging by both sieving and bridging mechanisms, which occurs independently across the parallel channels. Single particle clogs are formed downstream of the channels and towards the outlet while clogs formed by bridging or adhesion are located upstream and held in position by force chains. However, above a critical threshold, flow driving pressure overcomes force chains that would otherwise hold a bridged clog in place. Such behavior has been extensively reported in the flow and clogging of granular materials[37–39]. The magnitude of force chains is well characterized in diverse granular flow systems and their stability is known to determine the strength of a clog[40,41].

Similar to granular flows and collective dynamics, the role of force chains in colloidal clogging is demonstrated in the intermittent clogging, buckling, and flow of suspended particles through abrupt constrictions. The extent of flow intermittency or propensity to clog depends on the flow condition in such systems[14,20]. In the current study, we provide fundamental insights into the combined effects of flow driving pressure and particle volume fraction on the probability of clogging in a converging flow geometry that tapers over multiple length scales. We demonstrate an interplay between flow and suspension conditions, regulating the size and location of clogs in tapered channels. Understanding the mechanics of colloidal clogging in such geometry can facilitate the optimized design of microfilters and dispensing systems such as nozzles.

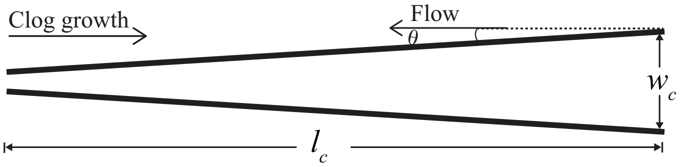

Fig. 1 Schematic illustration of a tapered channel. The 165 channels are identical, arranged in parallel, and tethered to an inlet reservoir. The width of each channel, w_c, tapers at an angle of $\theta \approx 0.02°$ over a length, $l_c \approx 5$ cm. In each channel, w_c decreases along the flow path – from 40 μm in the inlet to 4μm at the outlet. Flow is simultaneously delivered into each channel from the inlet reservoir. The discontinuous clogging process begins from the outlet, where the channels width is approximately equal to the flowing particle size. Due to the taper angle being very gentle: $\theta \approx 0.02°$, this figure is not drawn to scale.

2 Materials and Methods

2.1 Microfluidic Design and Flow Tests

The microfluidic device contains 165 parallel tapered channels, all connected to an inlet reservoir. The width of each channel is $w_c = 40$ μm at the inlet. It tapers to 4 μm at the outlet over a length $l_c \approx 5$ cm, at an angle $\theta \approx 0.02°$ (Fig. 1; not to scale). The channels are $\sim$10 μm deep, allowing up to two layers of particle packing in each clog. The microfluidic devices are fabricated with polydimethylsiloxane (Dow SYLGARD$^{\text{TM}}$ 184) using standard soft lithography methods. The elastomer base and curing agent are mixed in the ratio 8:1, and allowed to cure in an oven at 65°C. The surface of the device containing the channels is plasma cleaned and bonded on a microscope glass slide. The glass slides are also plasma cleaned before bonding. This treatment makes the surfaces of the channels hydrophilic. Hydrophobicity returns to the PDMS device on a time scale of hours after plasma treatment[42]. Therefore, devices are used immediately upon bonding.

Fluorescent polystyrene particles are used as received from Bangs Labs, suspended in water at 1% solids. The particles are monodisperse and have a mean diameter, $d_p \approx 4$ μm. They are slightly negatively charged, with zeta potential, $\zeta = -8.2 \pm 0.9$ mV (Anton Paar Litesizer 500). They are suspended in pure DI water, and do not aggregate over the duration of the flow test (see Fig. S1 in SI). The density of the particles (ρ_p) is $\sim$1.06 g$\cdot$cm^{-3}, which is approximately equal to the density of water, the suspend-

https://doi.org/10.26434/chemrxiv-2023-nfmkc-v2 ORCID: https://orcid.org/0000-0002-9773-6748 Content not peer-reviewed by ChemRxiv. License: CC BY 4.0

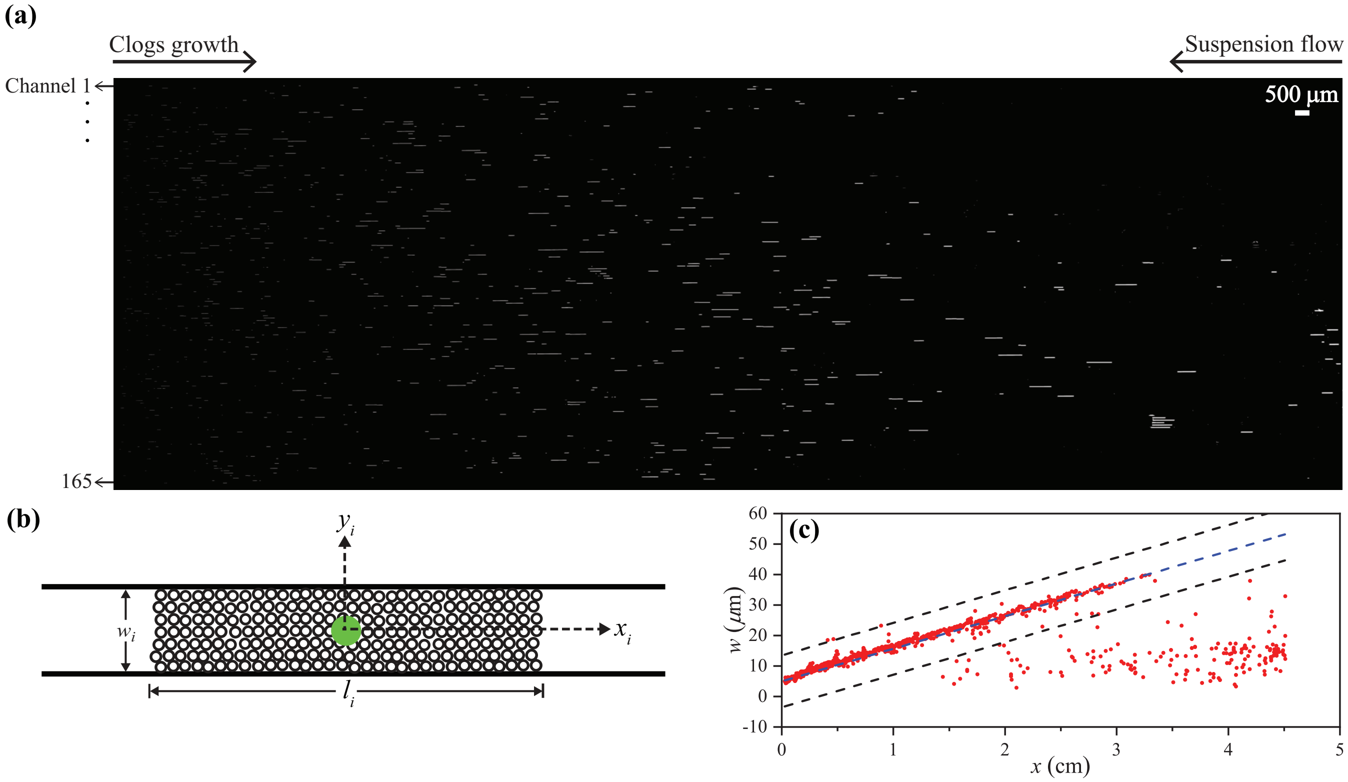

Fig. 2 (a) Micrograph of a clogged device demonstrating the discontinuity of clog growth from the channel outlets, on the left, to the inlet area, on the right. The fluorescent clogs formed during a flow test where ΔP = 700 mbar and ϕ = 0.10%. (b) Measurement protocol. The length (l), width (w), and centroid (x, y) of each clog are identified. (c) Scatter plot of w versus x. As illustrated in Fig.1, $x = 0$ cm at the outlet of the tapered channels while $x \geq 4$ cm in the inlet area. The line of best fit ($w \sim x$) confirms the channel taper angle $\theta \sim 0.02°$. Clogs located beyond $w(x) \pm 2d_p$ are not considered in the analyses.

ing fluid. Sedimentation is therefore negligible. We prepare dilute suspensions in DI water, at volume fractions (ϕ) in the range [0.005, 0.25%].

We flow the dilute suspensions through the microfluidic device at constant driving pressures (ΔP) in the range [200, 2000 mbar] using a a Fluigent LineUp Flow EZ^{TM} device. The Flow EZ applies a constant pressure to a reservoir containing the suspension. The flowrate (Q) is measured with a flow meter (Fluigent FLOW UNIT^{TM}).

A new device is used for each flow test, which typically runs for ∼25 minutes. Before a suspension flow test, pure water is first flowed through the microfluidic device at different ΔP while measuring Q. This procedure allows us to determine the hydraulic resistance (R_H) of the devices, and ensure they are in proper working condition. The plot of Q *vs.* ΔP is linear, and the hydraulic resistance R_H is the reciprocal of the slope. The linearity of Q *vs.* ΔP shows the microfluidic devices do not deform in the range of ΔP investigated in this study, indicating the channels behave as rigid walls[4].

In one set of measurements, the values of ΔP used are 200, 500, 700, 1000, 1200, 1500, and 2000 mbar. For this "Batch 1", $R_H = 80 \pm 5$ mbar·min·μL^{-1} for all devices used. We duplicate the entire set of measurements in a "Batch 2", using ΔP = 200, 500, 700, 900, 1200 and 1700 mbar. For Batch 2, $R_H = 75 \pm 6$ mbar·min·μL^{-1} for all devices used. Furthermore, the particles used in the Batch 2 experiments come from a separate batch obtained from the same supplier (Bangs Labs). In Batch 2, there is a slight reduction in the total number of clogs. This may be due to the ∼ 6% decrease in R_H combined with the different batch of particles. However, the qualitative behavior and conclusions regarding clogging remain the same.

We refer to the above device preparation as "pristine flow tests," in which particles are suspended in pure water and the channels surfaces are treated by plasma cleaning only. In a subset of flow tests, particles are dispersed in a 1 M NaCl solution to screen out electrostatic repulsion between particles. This induces both particle aggregation and deposition on the channel walls. In these flow tests, particles aggregate, deposit and clog upstream in the channels, in the widest portions of the channels and in the inlet area (see Videos S1 and S2 in SI). In another subset of flow tests, pristine channels are pretreated by flushing 5% CTAB through a device for at least 5 minutes before running the flow test. The CTAB prewash induces electrostatic attraction between the particles and the channel walls, causing particle deposition at the inlet of the channels (see Video S3 in SI). We also run one flow test after using a preflush of Aquapel^{TM} to make the surface hydrophobic[43]. Interestingly, making the channel surfaces hydrophobic does not change the clogging process (see Fig. S2 in SI).

https://doi.org/10.26434/chemrxiv-2023-nfmkc-v2 **ORCID:** https://orcid.org/0000-0002-9773-6748 Content not peer-reviewed by ChemRxiv. **License:** CC BY 4.0

2.2 Analyses of Clog Distributions

2.2.1 Image Analysis

The microfluidic devices are imaged on a Leica DMi8 microscope after each flow test to measure the positions and dimensions of each clog. The area of the channels is divided into several smaller regions, each covering an area of ∼2.5 mm by ∼2.5 mm. Images of these regions are tiled and processed to eliminate noise before analysis using a custom routine written in MATLAB.

Fig. 2a is a tiled and analyzed image of the clogged 165 microchannels for a flow test conducted with $\Delta P = 700$ mbar and $\phi = 0.10\%$. The image demonstrates the presence of multiple distinct clogs in each channel, indicated by bright spots or streaks in the image. For each clog, the width w, length l and centroid (x, y) are measured (Fig. 2b). See Fig. S3 in SI for tiled images of clogged channels from other conditions of ΔP and ϕ.

Since clogs span the width of the constriction, the clog width equals the channel width, $w = w_c$. Due to the tapered angle, $w(x) = w_o + (2\tan\theta)x$, where $w_o \approx 4$ μm and $x = 0$ cm indicates the channel outlet. Presented in Fig. 2c is a scatter plot of w as a function of x for the clogs shown in Fig. 2a. The line of best fit confirms $\theta \approx 0.02°$. However, $w \ll w_c$ for some bright spots or streaks in the tiled image. These are particles in the channels which are not associated with a clog. Objects outside the range $w(x) \pm 2d_p$, shown by the dotted lines, are therefore not included in the spatial distribution analyses. In Fig. 2, there are 166 bright spots not associated with clogs. This corresponds to a percentage, $\alpha \approx 15\%$, of the total number of bright spots or streaks; the vast majority of which, ∼85%, represents discontinuous clogs.

As seen in Fig. 2a, the bright spots corresponding to clogs occur within the channels in pristine flow tests. However, after flow tests with particles in NaCl solution or with CTAB pretreatment, bright pixels representing particles or clogs appear mainly in the inlet region, not in the channels. The ratio β quantifies the percentage of particle clogs, or bright pixels, found within the channels. That is, $\beta = 100\%$ means all particles or clogs are found in the channels after a flow test, while $\beta = 0\%$ means all particles or clogs are found in the inlet reservoir.

3 Results & Discussion

In non-tapered parallel microchannels, clogs in each channel grow continuously from their starting points and approximately the same length towards the inlet area. However, clogs formed in the tapered microchannels discussed in this study are discontinuous and spatially distributed across each parallel channel.

The number of clogs N formed in the microfluidic device under different conditions of ϕ and ΔP is presented in Table 1. Generally, more clogs form in higher conditions of ϕ and ΔP[21]. Compared to ΔP, ϕ has a greater effect on the rate of clogging. An order of magnitude variation in ΔP and ϕ does not produce similar effects on N. Increasing ΔP from 200 to 2000 mbar increases N by ∼40-50%. However, N increases by a factor of ∼2 or more for all ΔP when ϕ increases by an order of magnitude from 0.01 to 0.10%. Increasing either ΔP or ϕ delivers more particles to the microchannels over the course of the flow test, thus also increasing N. See Fig. S4 and Table S1 in SI for a comparison of the frequency of clogging in Batch 1 and Batch 2. In both, ϕ increases the clogging frequency at a rate higher than ΔP.

Table 1 Number of clogs N for different conditions of ΔP and ϕ.

ΔP (mbar)			ϕ (%)		
	0.005	0.01	0.05	0.10	0.25
200		357	587	728	
500		159	708	822	
700		442	812	860	
1000	473	477	754	908	1177
1500		521	1044	1023	
2000	517	498	816	1111	

3.1 Driving Pressure Increases Clog Lengths

Presented in Fig. 3 are box plot distributions of the length of the longest 10% of the discontinuous clogs formed in different conditions of ΔP and ϕ. The longest 10% is defined by the maximum length, $\bar{l}_{max}$, in each condition. All clogs with $\bar{l} > 0.9 \cdot \bar{l}_{max}$ are shown. Because the total number of clogs increases with ΔP, the number of longest clogs also increases as ΔP increases. Clog length is normalized by particle diameter, $\bar{l} = l/d_p$, which indicates the number of particles along the length of a clog. Boxes are drawn from the first to the third quartile, with the horizontal line indicating the mean value. See Fig. S5 in SI for the widths of the longest clogs ($\overline{w} = w/d_p$) and Fig. S6 for box plot distributions of $\bar{l}$ and $\overline{w}$ for all clogs in each condition.

As seen in Fig. 3a-c, increasingly longer clogs are formed as either ΔP or ϕ increases. Each panel shows $\bar{l}$ as a function of ΔP for a different ϕ condition. When $\phi = 0.01\%$ (Fig. 3a), $\bar{l}$ increases monotonically with ΔP. At $\Delta P = 200$ and 500 mbar, even the longest clogs are all less than $\bar{l} \approx 130$. $\bar{l}$ grows beyond 350 and up to 750 when $\Delta P = 2000$ mbar. As ϕ increases (Fig. 3b and c), $\bar{l}$ still increases with ΔP. However, now an apparent plateau appears at low ΔP. Below $\Delta P = 900$ mbar, $\bar{l}$ does not exceed ~ 350 at either $\phi = 0.05$ or 0.10%. Beyond $\Delta P = 900$ mbar, $\bar{l}$ grows significantly, with the longest clogs increasing from $\bar{l} \approx 600$ to 900 when $\phi = 0.05\%$, and up to 1400 when $\phi = 0.10\%$. Thus, it appears there are two regimes of ΔP, which also manifests in measurements of flowrate decay dynamics[4].

Since more clogs are formed as ΔP increases (Table 1), the data in Fig. 3a-c suggests a general trend of the formation of *more and longer* discontinuous clogs as ΔP is increased for each condition of ϕ.

3.2 Volume Fraction Moves Longest Clogs Upstream

The combined effect of ΔP and ϕ on clog dimension and location is readily seen in the scatter plots in Fig. 4. Each data point represents a clog. Normalized clog length $\bar{l}$ is plotted versus clog centroid position x. x represents the direction of clog growth: the origin $x = 0$ cm is the location of the channel outlets; the inlet area is located at $x = 4$ cm. That is, data points to the left within each figure represent clogs nearer the outlet, downstream, while data points to the right within each figure represent clogs nearer the inlet, upstream. The y axis location of each data point represents clog length. Each row of plots represents a constant ΔP condition while ϕ is varied in each column. The top two rows in Fig. 4 show

https://doi.org/10.26434/chemrxiv-2023-nfmkc-v2 **ORCID:** https://orcid.org/0000-0002-9773-6748 Content not peer-reviewed by ChemRxiv. **License:** CC BY 4.0

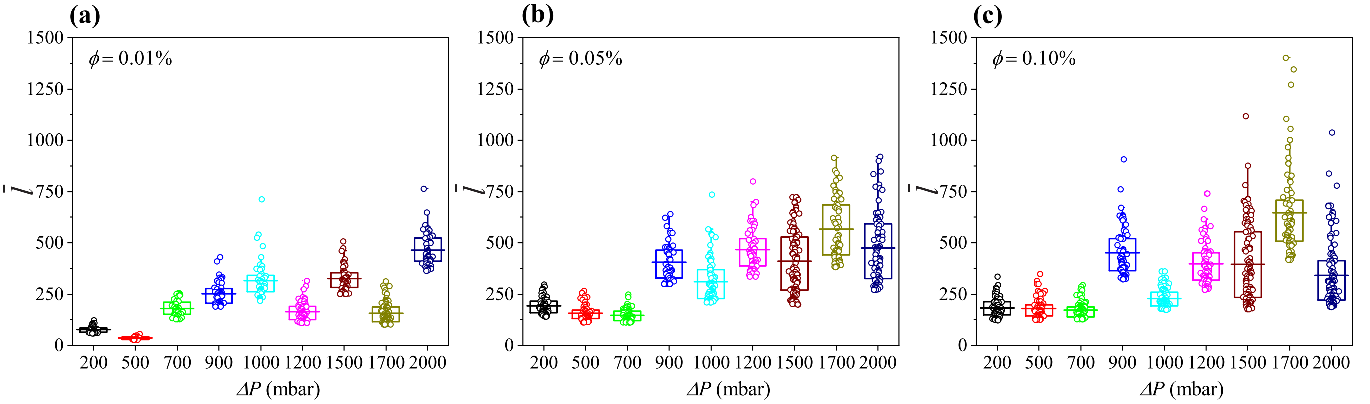

Fig. 3 Box plot distributions of clog dimensions, showing the effects of ΔP and ϕ on the normalized length $\bar{l}$ and width $\overline{w}$ of the longest 10% of the discontinuous clogs. (a) - (c) show longer clogs are formed as both ΔP and ϕ are increased. The spread of the distribution of $\bar{l}$ also tends to increase. For each ϕ, there seems to be a critical ΔP around 900 mbar, beyond which the average $\bar{l}$ increases by a factor of 2. Note that the ΔP axis is not on a linear scale.

$\Delta P = 200$ and 700 mbar conditions while the bottom row shows ΔP = 2000 mbar. From left to right across these rows, the number of clogs increases with ϕ, providing a visual representation of the trends in Table 1.

Relatively short clogs are formed in low ϕ and ΔP conditions, as seen in Fig. 4a. These clogs are positioned downstream, at small x, towards the outlet of the channels. As ϕ increases, the additional clogs appear at larger x, upstream toward the inlet area. This can be seen in the progression of the scatter plots from left to right in all three rows, for each ΔP condition. However, increasing ϕ in low ΔP conditions does not appreciably increase $\bar{l}$: for instance, most clogs formed at $\Delta P = 200$ and 500 mbar (Figs. 4a-f) remain below $\bar{l} = 200$, with only one clog longer than $\bar{l} = 300$.

In contrast to the effect of ϕ, as ΔP increases, the overall position of the clogs does not change dramatically, as can be seen by looking down each column. However, $\bar{l}$ for the longest clogs does increase dramatically with ΔP, regardless of ϕ. This is seen most clearly when $\Delta P = 2000$ mbar, in the third row of Fig. 4: the longest clogs reach $\bar{l} = 800$ or higher for all three values of ϕ. In the most dilute suspensions, $\phi = 0.01\%$ (Figs. 4a, d, g), the discontinuous clogs grow longer in downstream positions of the tapered channels as ΔP increases. When ΔP = 2000 mbar and ϕ = 0.01% (Fig. 4g), the longest clogs ($\bar{l} \approx 400$) are located at $x \lesssim 1$ cm. In this most dilute case, particles travel further down a channel to grow a downstream clog before a new clog is formed upstream.

Visualizing the clog lengths in the scatter plots of Fig. 4. provides position information that cannot be seen in Fig. 3. As ϕ increases, additional clogs form nearer the inlet ($x > 2$ cm) for each ΔP. But, interestingly, at the highest ΔP, Fig. 4g-i shows that it is the *longest* of the clogs that appear further upstream as ϕ increases. This ϕ-dependent shift in the position of the longest discontinuous clogs is observed when $\Delta P \gtrsim 1000$ mbar (see Fig. S7 in SI for other ΔP cases).

These combined observations of clog length and position describe particle transport during a flow test. Not only do longer clogs form at higher ΔP, but their location depends on ϕ. Particles travel further downstream at the lowest ϕ. Increasing ϕ prevents some degree of particle transport downstream.

3.3 Probability of Clogging

Clogging tendencies have been measured in diverse flow systems: colloidal flows,[20] granular flows[19] and crowd dynamics[44]. In systems with discrete variables, clogging probabilities are assessed by collecting data over a range of geometric parameters, varying either w_c and/or d_p in separate experiments. Then, clogging probability refers to the number of clogs that occur divided by the total number of experiments performed[45,46].

In the flow tests described here, w_c/d_p varies continuously within a single device. The effect of geometry on clogging can be assessed simply by investigating different regions of a single fluidic device. Here, clogging is described by the survivor functions of the empirical analyses. These are complements of the cumulative distribution function. They can describe the decreasing probability of clogging with increasing w_c/d_p[19] and the sensitivity of burst sizes to the presence of obstacles in flow systems that clog intermittently[14,44]. The effect of ΔP and ϕ on the clogging process can be investigated by examining the survivor functions in different experimental conditions.

Presented in Fig. 5 are the survivor functions of the empirical data for different conditions of ΔP and ϕ. $P(\overline{W} > \overline{w})$ represents the probability of finding a clog that is *at least* $\overline{w}$ wide while $P(\bar{L} > \bar{l})$ represents the probability of finding a clog that is *at least* $\bar{l}$ long. When $P = 1$, all clogs are $\overline{W} > \overline{w}$ or $\bar{L} > \bar{l}$; essentially, the probability of clogging is 100%. As $\overline{w}$ or $\bar{l}$ increase, fewer clogs are found that meet the criteria, and the probability of finding a clog P decays. Interestingly, the shapes of the survivor function curves in Fig. 5 are reminiscent of survivor functions obtained in a system of active, flagellated swimmers jamming a microfluidic bottleneck constriction, reflecting a similarity in the underlying statistical processes[47,48].

Clogging probability in specific channel width positions strongly depends on ϕ. For fixed ΔP = 1000 mbar, Fig. 5a shows that $P(\overline{W} > \overline{w})$ increases with increasing ϕ for almost the entire range of $\overline{w}$. Convergence is observed only where $\overline{w} = 1$, indicating

https://doi.org/10.26434/chemrxiv-2023-nfmkc-v2 **ORCID:** https://orcid.org/0000-0002-9773-6748 Content not peer-reviewed by ChemRxiv. **License:** CC BY 4.0

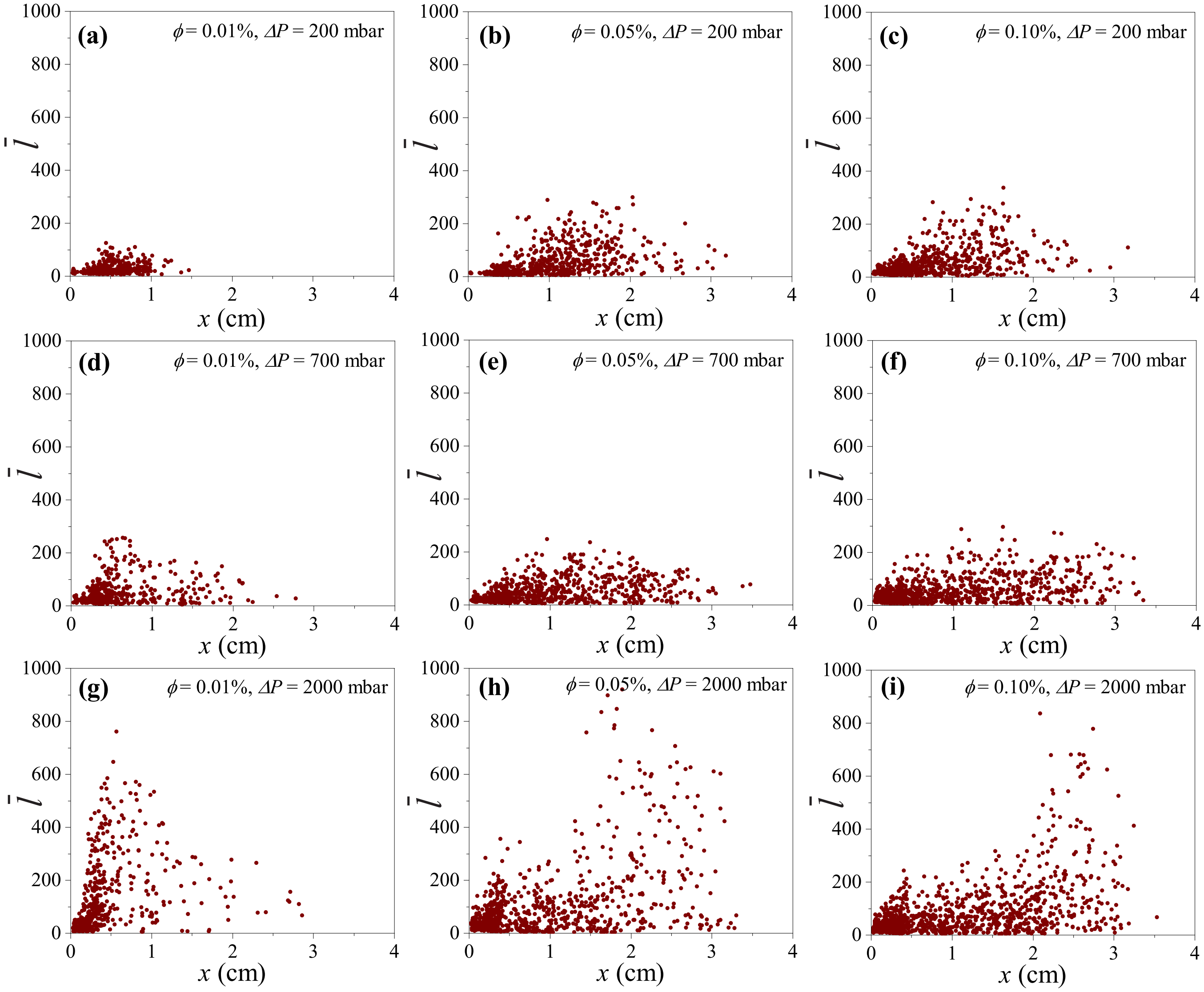

Fig. 4 Scatter plots of normalized clog lengths $\bar{l}$ versus their location in the x-axis of the Cartesian plane. $x = 0$ cm corresponds to the outlet of the tapered channels, $x = 2$ cm is approximately the midpoint while $x = 4$ cm in the inlet area, as illustrated in Fig. 1. A different condition of constant ϕ is presented in each column while ΔP is varied in each row. It shows the longest clogs are positioned downstream of the channels ($x < 2$ cm) as ΔP increases; but increasing ϕ shifts their location more upstream ($x > 2$ cm).

the channel outlet, and in positions closest to the channel inlet, where $\overline{w} \geq 9$. For $\phi = 0.005$ and 0.01%, 90% of the discontinuous clogs are narrower than $\overline{w} = 4$. As ϕ increases to 0.1 and 0.25%, the widest 10% of the clogs surpass $\overline{w} = 8$. Higher probability of wider clogs with increasing ϕ is due to the increase in clogging frequency with increasing ϕ (Table 1). Frequent truncation of clog growth and initiation of new clogs in each channel leads to the formation of clogs upstream in wider regions of the channels ($w \sim x$). As a point of comparison, the probability of rigid granular particles clogging a hopper vanishes as $\overline{w} \to 6$[19,49]. However, $P(\overline{W} > \overline{w})$ shows no strong dependence on ΔP (see Fig. S8 in SI).

Clogging probability as a function of clog length does not have any strong analogies in the clogging literature, due to the uniqueness of the discontinuous clogs discussed here. Investigating the probability of clogs as a function of length corroborates the trends seen in Figs. 3 and 4. Fig. 5b shows $P(\overline{L} > \overline{l})$ for six values of ΔP, with ϕ fixed at 0.10%. In the region where $\overline{l} \leq 100$, there is a slight non-monotonic dependence of $P(\overline{L} > \overline{l})$ on ΔP. But, generally, the likelihood of relatively short clogs is between ~70-90% for $\overline{l} \leq 100$. However, significant effects of varying ΔP are observed where $\overline{l} > 100$. Beyond $\overline{l} = 100$, the three lower ΔP traces remain collapsed on each other. The probability of lengthy clogs, $P(\overline{L} > 400)$, however, is demonstrably higher when $\Delta P > 1000$ mbar. While Fig. 5 represents Batch 1, the presence of a critical ΔP matches the observations in Fig. 3, which represents both batches.

$P(\overline{L} > \overline{l})$ does not depend strongly on ϕ. This can be seen at fixed $\Delta P = 1000$ mbar (see Fig. S8 in SI). The curves for $P(\overline{L} > \overline{l})$ significantly overlap for all five values of ϕ examined. The formation of relatively short clogs ($\overline{l} < 100$) is equally likely for all ϕ. However, differences are observed beyond $\overline{l} = 100$. Clogs grow longer in dilute conditions ($\phi = 0.005\%$) compared to more

https://doi.org/10.26434/chemrxiv-2023-nfmkc-v2 **ORCID:** https://orcid.org/0000-0002-9773-6748 Content not peer-reviewed by ChemRxiv. **License:** CC BY 4.0

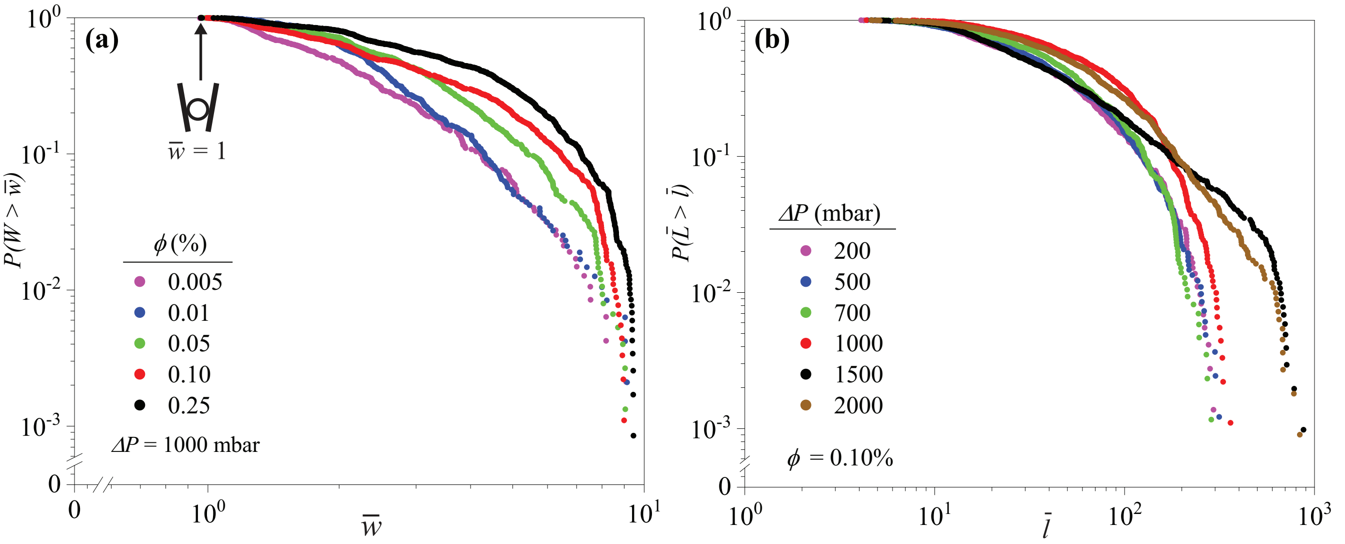

Fig. 5 Complementary cumulative distribution functions for the distributions of clog widths ($\bar{w}$) when (a) $\Delta P = 1000$ mbar and clog lengths ($\bar{l}$) when (b) $\phi = 0.10\%$. Inset in (a) is a schematic representation of a $\bar{w} = 1$ clog; a single particle clog. The plots show the probability of wide clogs increases with increasing ϕ due to increased incidence of clog truncation and initiation events while the probability of long clogs increases with increasing ΔP.

concentrated cases (ϕ = 0.10 and 0.25%).

3.4 Clogging Mechanism

In this study, particles travel through the tapered channels towards the outlet, where the discontinuous clogging process begins. Clogs are formed by sieving at the outlet where $w_c \approx d_p$ (see Video S4 in SI). Clogs can be formed by bridging in positions where $w_c > d_p$ [20,21]. This is readily observed up to $w_c \approx 4d_p$ (see Video S5 in SI).

Table 2 Estimated number of particles delivered into one tapered channel *per* second, n, in different conditions of ΔP and ϕ. During a constant ΔP flow test, n decreases with time due to clogging and flowrate decay. n_0 and $n_{1/2}$ are the initial and half-time values. They are estimated from the flowrates $Q(t)$ at $t = 0$ and $t = 12.5$ min, which are reported in Ref. [4]. $n = \phi Q(t)/165V_p$, where V_p is the volume of a spherical particle.

ΔP (mbar)	ϕ (%)		
	0.01	0.05	0.10
	n_0, $n_{1/2}$	n_0, $n_{1/2}$	n_0, $n_{1/2}$
200	0.5, 0.03	2.79, 1.01	7.37, 1.94
500	1.21, 0.82	7.50, 2.99	15.74, 4.51
700	2.27, 1.10	9.95, 3.35	25.73, 6.22
1000	3.42, 1.00	16.52, 3.34	33.41, 5.59
1500	5.38, 1.46	27.20, 5.32	54.00, 10.65
2000	7.21, 1.46	38.85, 6.41	66.20, 11.33

In wider regions, where $w_c/d_p > 4$, clogging by bridging becomes less likely. Table 2 quantifies the flux of particles *per* channel for the entire range of ϕ and ΔP investigated. Each flow condition is described by both n_0 and $n_{1/2}$, where n_0 indicates the number of particles *per* time flowing through a single channel at the beginning of the flow test. Over time, as flowrate Q decays, so does the particle flux: $n_{1/2}$ estimates particle flux at the midpoint of the flow test, given previously reported measurements of $Q(t)$ [4]. At the largest values of ϕ and ΔP, n_0 exceeds 60 particles *per* second. But after half of the flow test has elapsed, the flux drops to $n_{1/2} = 11$ at maximum.

Table 3 Comparison between particle adhesion in pristine flow tests and conditions where adhesive interactions are chemically induced. The percentage of nonclogs (α) is an order of magnitude higher when adhesive interactions are induced, compared to pristine controls. The percentage of particles that reach the microchannels (β) also reduces in the presence of chemically-induced particle adhesion and deposition. Here, $\phi = 0.05\%$ in all cases.

Treatment	ΔP	α (%)	β (%)
Particles in 1 M NaCl solution	500	43.5	14.1
Particles in pure water	500	2.8	99.5
CTAB prewash	1500	37.4	6.1
Particles in pure water	1500	3.2	-

Given the low particle flux estimates, we investigate the possibility that particle aggregation or adhesion contribute to clogging in regions of the device where $w_c/d_p > 4$. In one flow test, we induce aggregation by suspending the particles in a 1 M NaCl solution. The presence of salt in suspension is known to induce aggregation and clogging in microfluidic colloidal suspension flows [50,51]. The ions screens away the electrostatic repulsion between particles and facilitates aggregation due to attractive van der Waals interactions. This can be seen readily in the inlet region as soon as the flow test begins (see Video S1 in SI). This treatment facilitates adhesion of the particles and aggregates to the channel walls.

A separate flow test features a case where the microfluidic device is prewashed with CTAB. This imparts a positive charge to the channel walls and attracts the slightly negatively charged particles. Again, this electrostatically induced adhesion is seen in the inlet region soon after the flow test begins (see Video S3 in SI). Previous studies also show the presence of strong adhesive interactions causes particles to deposit and clog upstream in the inlet area [29,50,52].

https://doi.org/10.26434/chemrxiv-2023-nfmkc-v2 **ORCID:** https://orcid.org/0000-0002-9773-6748 Content not peer-reviewed by ChemRxiv. **License:** CC BY 4.0

Both aggregation induced by salt and adhesion induced by electrostatics cause particles to stick to the device mainly in the inlet region; only very few travel downstream to clog the tapered channels. This behavior is qualitatively different than clogging in pristine flow tests. The comparison can be quantified by α and β, shown in Table 3.

The percentage of bright spots which are not clogs (α) is based on the analysis in Fig. 2c. It is the fraction of bright spots or streaks outside the $w(x) \pm 2d_p$ limit. The α fraction of bright spots are nonclogs; not associated with any clog in the microchannels and likely constituted by individual particles adhered to the channel walls, even in pristine flow tests. There is, approximately, an order of magnitude increase in α in both conditions where deposition is induced, compared to pristine controls (Table 3). Only $\sim$3% of the clogs are nonclogs in pristine flow tests. However, α is more than 35% where aggregation or adhesive interactions are induced.

The percentage of all clogs found in the channels compared to the entire device is given by β. The quantity $100 - \beta$ indicates the percentage of bright pixels found in the inlet reservoir. As shown in Table 3, less than 15% of the fluorescent particles are found in the microchannels in cases where adhesive interactions are induced; the majority are located in the inlet reservoir. The particles deposit and clog in the inlet of the channels, and grow into the inlet reservoir (see Videos S1 and S3 in SI). However, this phenomenon is not observed in pristine flow tests, where more than 90% of the particles are located in the microchannels (Table 3). Together, the measurements in Table 3 provide evidence that adhesion observed in pristine flow tests occurs to a much lower degree, and is not due to aggregation or electrostatic attractions.

In short, the comparison between the pristine flow tests, those with NaCl, and those with CTAB suggest two main conclusions. Particle-particle aggregation is nearly negligible in the pristine tests: the slightly negative surface charge likely provides a sufficient energetic barrier against aggregation. Further, adhesion in the pristine tests does happen, but much more rarely than when interactions are dominated by van der Waals or electrostatic attraction. In pristine flow tests, particles do not stick in the inlet region. Any adhesion is qualitatively different from that observed when the particles are suspended in a salt solution (see Video S1 in SI) or when electrostatic attractions are induced between the particles and channel walls (see Video S3 in SI). When electrostatic repulsion is screened away and van der Waals attractions dominate, adhesion is severe[50,51]. Adhesion events do still occur even in pristine tests, but to a minimal degree. This suggests that van der Waals forces are not negligible, even in pristine conditions.

Even though adhesion events occur more rarely in the pristine flow tests, they have important consequences, and may eventually lead to clog formation. In pristine flow tests, video evidence suggests that there are instances in wider parts of the device ($w_c/d_p > 5$) where a discontinuous clog can be initiated due to the adhesion of a single particle to the channel (see Video S6 in SI). In the video, five individual particles can be seen sticking to the device, each in a different channel. However, individually adhered particles may or may not result in a clog. In the video, only one of the five leads to a complete clog. Further, more than two minutes elapses between the first individual particle deposits and the time at which the channel is completely clogged. Often, particles simply flow past a stuck particle. There are even instances where a downstream clog can grow over and past particles already deposited within a channel (see Video S7 in SI).

3.5 Existence of a Critical Pressure

The above results and analysis may suggest the presence of a critical pressure near $\Delta P \approx 900 - 1000$ mbar. As seen in Figs. 3–5, above this ΔP, clogs grow dramatically longer. At $\phi = 0.01\%$, the lengthening of clogs appears gradual (Fig. 3). But at higher volume fractions, $\phi = 0.05$ and 0.10 %, this lengthening occurs after a low-pressure plateau below $\Delta P = 900$ mbar, and is more dramatic (Figs. 3b and c). The location of these long clogs, in turn, depends on ϕ, with the most dilute conditions facilitating particle transport to lengthen downstream clogs. This ability of clogs to grow significantly longer at higher ΔP may suggest that pressure can disrupt the process of clogging. Lower ΔP conditions form many short clogs, particularly in higher ϕ conditions. Higher ΔP can disrupt potential clog formation, sending individual particles downstream to lengthen existing clogs.

Critical ΔP or forces are known to disrupt clogging in other contexts. The existence of a critical ΔP is seen in flows of individual soft particles through a constriction slightly narrower the particle diameter. The translocation pressure required to dislodge a soft particle increases linearly with the particle elasticity and scales with a dimensionless confinement ratio of particle diameter to constriction width[53].

Force chains in *potentially jamming* oil-in-water droplets are estimated to be on the order of 1 μN in a quasi 2-D emulsion[45]. Experiments and simulations have been used to investigate collective dynamics of particles during arch formation as a function of inter-particle interactions[18,23,54]. Force chains and frictional contact stresses dominate clog formation in the absence of cohesive or adhesive interactions[24,55]. Force chains in colloidal suspensions and granular flows near the jamming transition have been visualized extensively using both experiments and simulations. However, quantitative measurements of force chains in clogging of colloidal suspensions are less well-explored.

Building on these concepts of force chains and translocation ΔP, we can use the critical ΔP to estimate the force required to disrupt a clog or prevent it from forming. This critical ΔP represents a force divided by the cross sectional area of all the channels. The channel depth is $\sim$10 μm throughout the device, channel width narrows from 40 down to 4 μm. There are 165 channels which are each subject to ΔP due to their arrangement in parallel. If $\Delta P_{\text{crit}} \approx 1000$ mbar balances the force across a single clog spanning the entire channel width, this suggests that particular clog can sustain $\approx 4 - 40$ μN. This estimate is most appropriate if there exists a single clog along the length of a channel. The presence of multiple discontinuous clogs along the flow direction would reduce this estimate. Still, 1μN is the same order of magnitude as that observed in a jamming of a quasi 2-D emulsion[45]. However, this estimate is an upper limit, acknowledging that the

https://doi.org/10.26434/chemrxiv-2023-nfmkc-v2 **ORCID:** https://orcid.org/0000-0002-9773-6748 Content not peer-reviewed by ChemRxiv. **License:** CC BY 4.0

pressure losses in the flow direction are affected by the presence of the clogs. In narrower regions of the channels, where bridging is possible, existence of a critical ΔP may represent disruption of a simultaneous bridging event. However, in wider regions of the channels, where clogging may be facilitated by a single adhered particle, this pressure may represent prevention of the final particle or particles to complete the clogging arch.

It is worth noting that, once formed in the tapered channels, clogs are not later disrupted, even at high ΔP. This can be seen in microscopy videos of clog growth obtained during a typical flow test (see Videos S4 and S5 in SI). Neither gradual nor abrupt increases in ΔP can dislodge clogs, not even when the pressure is suddenly increased from 500 to 2000 mbar (see Videos S8 and S9 in SI). Not even flow reversal dislodges the clogs (see Video S10 in SI). In all cases, clogs grow discontinuously, and remain stable for the duration of the flow tests. Therefore, the concept of clog prevention at high ΔP suggests there is a moment in which particles may or may not form a bridge. Indeed, recent experiments and simulations reveal transient clogging of colloids navigating an abrupt constriction; these clogs can have infinitesimal lifetimes[14,16]. But, once formed, these clogs are remarkably stable. Interestingly, this observation contrasts those in which perturbation can be used to dislodge a clog, as in hopper flows or silo discharge[56].

The suggestion that increasing ΔP disrupts force chains may also explain the somewhat counter-intuitive results in Table 1. That is, increasing ϕ by an order of magnitude increases the number of clogs N by a factor of 2 – 5. However, ΔP has a much weaker effect: increasing ΔP by an order of magnitude increases N by barely 50%. This less dramatic increase may be due to the disruption of force chains. Increasing ΔP certainly sends more particles into the channels, as seen in Table 2, but these do not all form new clogs. Consequently, N does not increase as strongly with ΔP compared to ϕ. In addition, increasing ϕ may somewhat reduce the ability of high ΔP to prevent clog formation. When ΔP is high and ϕ is low, clog prevention occurs very effectively upstream: the longest clogs are found downstream, where $x < 1$ cm, as seen in Fig. 4g. However, as ϕ increases, the longest clogs are upstream, near $x = 3$ cm, towards the channel inlet area.

The observations suggest a competition between ΔP and ϕ. That is, the combination of clogging frequency, clog lengths, and positions suggests an increasing probability of *more but shorter* clogs as ϕ increases and *more and longer* clogs as ΔP increases. So, while high ΔP may destabilize force chains in incipient *about-to-form* clogs, increasing ϕ appears to stabilize them.

4 Conclusions

The dimensions and locations of discontinuous clogs in tapered microchannels are controlled by flow conditions. Two regimes of driving pressure emerge. Clog lengths are short and relatively independent of volume fraction in the low driving pressure regime but much longer clogs form in a high driving pressure regime. In contrast, increasing particle volume fraction increases the frequency of clogging, allowing clogs to form upstream, in regions where the microchannels are wider.

While driving pressure controls clog length, particle volume fraction controls clog width and location. There is a ϕ-dependent shift in the location of clogs in the tapered channels. The longest clogs are positioned downstream of the channels when the flow driving pressure is high and particle volume fraction is low. However, increasing particle volume fraction shifts the location of the longest clogs upstream. Long discontinuous clogs are only formed in less constricted areas of the channels, as volume fraction increases. As a result, the force chains that must be overcome to grow long clogs increase substantially as particle volume fraction increases.

Furthermore, our results suggest a more nuanced understanding of the three primary clogging mechanisms typically discussed in the context of colloidal clogging. As expected, clogging by bridging is observed in regions of the tapered channels that span several particle widths. However, in wider regions of the channels, the probability of clogging by bridging decreases, especially due to low particle flux conditions. Interestingly, clogs still occur in regions of the channel up to 9 particles wide. Even in pristine conditions, single particle adhesion events can occur, likely induced by van der Waals forces rather than electrostatics. These events are sometimes observed to provide a nucleation site for a clog to eventually fill the cross-section in these wider regions of the channels. The appearance of the critical pressure, therefore, may reflect the driving pressure overcoming or preventing either the force chains across a simultaneously formed bridge *or* the force chain that would be formed by the final particle(s) to reach and complete a clogging arch.

The results presented in this study demonstrate the significance of confinement geometry on clogging processes. Understanding features of suspension flow through tapered channels can help in the design of filters with extended lifespans. Also, a tapered geometry summarizes flow and clogging behavior in systems where the flow cross section narrows over multiple length scales. Examples are found in blood circulation, printer nozzles, and multistage filters designed to trap even the smallest suspended particles. In particular, the microfluidic device mimics systems where suspension flow is distributed from one source into multiple tapered streams.

Author Contributions

S.M.H. initiated and supervised the overall study. O.T.M. and S.M.H. conceived of the project and designed the plan of experiments and analyses. O.T.M. conducted the experiments and analyzed the results. O.T.M. and S.M.H. contributed to the discussion of the data and writing of the manuscript.

Conflicts of interest

There are no conflicts to declare.

Acknowledgements

The authors acknowledge funding from Northeastern University and Yale University Cleanroom for microfabrication assistance.

Notes and references

1 R. Zhang, Z. Yang, R. Detwiler, D. Li, G. Ma, R. Hu and Y.-F. Chen, *Geophysical Research Letters*, 2023, **50**,

https://doi.org/10.26434/chemrxiv-2023-nfmkc-v2 **ORCID:** https://orcid.org/0000-0002-9773-6748 Content not peer-reviewed by ChemRxiv. **License:** CC BY 4.0

e2022GL102097.
2 B. Dincau, E. Dressaire and A. Sauret, *Physics Today*, 2023, **76**, 24–30.
3 R. Hidalgo, A. Goñi-Arana, A. Hernández-Puerta and I. Pagonabarraga, *Physical Review E*, 2018, **97**, 012611.
4 O. T. Majekodunmi and S. M. Hashmi, *Scientific Reports*, 2022, **12**, 1–13.
5 A. Sauret, K. Somszor, E. Villermaux and E. Dressaire, *Physical Review Fluids*, 2018, **3**, 104301.
6 N. Delouche, B. Dersoir, A. Schofield and H. Tabuteau, *Physical Review Fluids*, 2022, **7**, 034304.
7 N. Debnath, A. Kumar, T. Thundat and M. Sadrzadeh, *Scientific reports*, 2019, **9**, 1–10.
8 S. Hashmi, M. Loewenberg and A. Firoozabadi, *Physics of Fluids*, 2015, **27**, 083302.
9 I. Bouhid de Aguiar, M. Meireles, A. Bouchoux and K. Schroën, *Scientific reports*, 2019, **9**, 3063.
10 J. Linkhorst, T. Beckmann, D. Go, A. J. Kuehne and M. Wessling, *Scientific reports*, 2016, **6**, 22376.
11 N. Debnath and M. Sadrzadeh, *Journal of the Indian Institute of Science*, 2018, **98**, 137–157.
12 N. Lu, H. M. Tay, C. Petchakup, L. He, L. Gong, K. K. Maw, S. Y. Leong, W. W. Lok, H. B. Ong, R. Guo *et al.*, *Lab on a Chip*, 2023.
13 A. Sauret, E. C. Barney, A. Perro, E. Villermaux, H. A. Stone and E. Dressaire, *Applied Physics Letters*, 2014, **105**, 074101.
14 M. Souzy and A. Marin, *Journal of Fluid Mechanics*, 2022, **953**, A40.
15 K. Sharp and R. Adrian, *Microfluidics and Nanofluidics*, 2005, **1**, 376–380.
16 P. Viot, G. Page, C. Barré and J. Talbot, *Physical Review E*, 2022, **105**, 014604.
17 A. Tordesillas and M. Muthuswamy, *Journal of the Mechanics and Physics of Solids*, 2009, **57**, 706–727.
18 E. Dressaire and A. Sauret, *Soft matter*, 2017, **13**, 37–48.
19 K. To, P.-Y. Lai and H. K. Pak, *Physical Review Letters*, 2001, **86**, 71–74.
20 M. Souzy, I. Zuriguel and A. Marin, *Physical Review E*, 2020, **101**, 060901.
21 N. Vani, S. Escudier and A. Sauret, *Soft matter*, 2022, **18**, 6987–6997.
22 N. Delouche, J. van Doorn, T. Kodger, A. Schofield, J. Sprakel and H. Tabuteau, *Journal of Membrane Science*, 2021, **635**, 119509.
23 G. C. Agbangla, P. Bacchin and E. Climent, *Soft Matter*, 2014, **10**, 6303–6315.
24 P. Prakash, A. Abdulla and M. Varma, *Langmuir*, 2021, **37**, 6915–6922.
25 D. Y. Kim, S. Y. Jung, Y. J. Lee, H. Jin and K. H. Ahn, *Separation and Purification Technology*, 2023, 124263.
26 B. Dersoir, M. R. de Saint Vincent, M. Abkarian and H. Tabuteau, *Microfluidics and Nanofluidics*, 2015, **19**, 953–961.
27 T. Knippenberg, A. Lüders, C. Lozano, P. Nielaba and C. Bechinger, *Scientific Reports*, 2022, **12**, 11525.
28 R. Jäger, M. Mendoza and H. J. Herrmann, *Physical Review Fluids*, 2018, **3**, 074302.
29 G. C. Agbangla, É. Climent and P. Bacchin, *Separation and purification technology*, 2012, **101**, 42–48.
30 S. Chen, W. Liu and S. Li, *Physical Review E*, 2016, **94**, 063108.
31 Q. Liu, B. Zhao and J. C. Santamarina, *Journal of Geophysical Research: Solid Earth*, 2019, **124**, 9495–9504.
32 T. v. d. Laar, S. t. Klooster, K. Schroën and J. Sprakel, *Scientific reports*, 2016, **6**, 1–8.
33 S. S. Massenburg, E. Amstad and D. A. Weitz, *Microfluidics and Nanofluidics*, 2016, **20**, 1–5.
34 M. Trofa, G. D'Avino and P. L. Maffettone, *Physics of Fluids*, 2021, **33**, 083320.
35 J. Yodh, V. Spandan and L. Mahadevan, *Physical Review Letters*, 2020, **125**, 044501.
36 B. P. Croom, A. Abbott, J. W. Kemp, L. Rueschhoff, L. Smieska, A. Woll, S. Stoupin and H. Koerner, *Additive Manufacturing*, 2021, **37**, 101701.
37 F. Nicot, H. Xiong, A. Wautier, J. Lerbet and F. Darve, *Granular Matter*, 2017, **19**, 18.
38 L. Zhang, N. G. H. Nguyen, S. Lambert, F. Nicot, F. Prunier and I. Djeran-Maigre, *European Journal of Environmental and Civil Engineering*, 2017, **21**, 874–895.
39 P. Guo, *Acta Geotechnica*, 2012, **7**, 41–55.
40 A. Abed Zadeh, J. Barés, T. A. Brzinski, K. E. Daniels, J. Dijksman, N. Docquier, H. O. Everitt, J. E. Kollmer, O. Lantsoght, D. Wang *et al.*, *Granular Matter*, 2019, **21**, 1–12.
41 R. Mandal, C. Casert and P. Sollich, *Nature Communications*, 2022, **13**, 4424.
42 T. Tsuzuki, K. Baassiri, Z. Mahmoudi, A. S. Perumal, K. Rajendran, G. M. Rubies and D. V. Nicolau, *Materials*, 2022, **15**, 2313.
43 A. R. Abate, D. Lee, T. Do, C. Holtze and D. A. Weitz, *Lab on a Chip*, 2008, **8**, 516–518.
44 I. Zuriguel, D. R. Parisi, R. C. Hidalgo, C. Lozano, A. Janda, P. A. Gago, J. P. Peralta, L. M. Ferrer, L. A. Pugnaloni, E. Clément *et al.*, *Scientific reports*, 2014, **4**, 7324.
45 K. W. Desmond, P. J. Young, D. Chen and E. R. Weeks, *Soft Matter*, 2013, **9**, 3424–3436.
46 S. Alborzi, D. Abrahamyan and S. M. Hashmi, *Physical Review E*, 2023, **107**, 024901.
47 E. Al Alam, M. Brun-Cosme-Bruny, V. Borne, S. Faure, B. Maury, P. Peyla and S. Rafaï, *Phys. Rev. Fluids*, 2022, **7**, L092301.
48 O. T. Majekodunmi and S. M. Hashmi, *Physics of Fluids*, 2023, **35**, 112007.
49 A. Janda, I. Zuriguel, A. Garcimartín, L. A. Pugnaloni and D. Maza, *Europhysics Letters*, 2008, **84**, 44002.
50 C. M. Cejas, F. Monti, M. Truchet, J.-P. Burnouf and P. Tabeling, *Langmuir*, 2017, **33**, 6471–6480.
51 C. M. Cejas, L. Maini, F. Monti and P. Tabeling, *Soft Matter*,

https://doi.org/10.26434/chemrxiv-2023-nfmkc-v2 **ORCID:** https://orcid.org/0000-0002-9773-6748 Content not peer-reviewed by ChemRxiv. **License:** CC BY 4.0

2019, **15**, 7438–7447.

52 D. Y. Kim, S. Y. Jung, Y. J. Lee and K. H. Ahn, *Langmuir*, 2022, **38**, 6013–6022.

53 Y. Li, O. S. Sarıyer, A. Ramachandran, S. Panyukov, M. Rubinstein and E. Kumacheva, *Scientific reports*, 2015, **5**, 17017.

54 Z. B. Sendekie and P. Bacchin, *Langmuir*, 2016, **32**, 1478–1488.

55 Y. Huang and K. E. Daniels, *Granular Matter*, 2016, **18**, 85.

56 I. Zuriguel, *Papers in physics*, 2014, **6**, 0–0.

https://doi.org/10.26434/chemrxiv-2023-nfmkc-v2 **ORCID:** https://orcid.org/0000-0002-9773-6748 Content not peer-reviewed by ChemRxiv. **License:** CC BY 4.0